Hindawi
Journal of Chemistry
Volume 2024, Article ID 9307714, 12 pages
https://doi.org/10.1155/2024/9307714

Research Article

Computational Evaluation of the Structural, Topological, and Solvent Effects on the Nonlinear Optical Properties of 1-Methylurea Butanedioic Acid Crystal

Stanley Numbonui Tasheh,[1] **Nyiang Kennet Nkungli**,[1] **Charly Tedjeuguim Tsapi**,[2] **Dodo Lydie Ajifac**,[1] **and Julius Numbonui Ghogomu**[1,2]

[1]*Department of Chemistry, Faculty of Science, The University of Bamenda, P. O. Box 39, Bambili, Bamenda, Cameroon*
[2]*Research Unit of Noxious Chemistry and Environmental Engineering, Department of Chemistry, Faculty of Science, University of Dschang, P.O. Box 67, Dschang, Cameroon*

Correspondence should be addressed to Stanley Numbonui Tasheh; stanleytash94@gmail.com and Julius Numbonui Ghogomu; ghogsjuju@hotmail.com

Received 12 April 2023; Revised 5 March 2024; Accepted 20 April 2024; Published 11 May 2024

Academic Editor: Mahmood Ahmed

In silico investigation of the effects of a molecule's framework and surroundings on its nonlinear optical (NLO) response is still an active topic of study in the fields of photonics and optoelectronics. NLO materials play a crucial role in modern photonics and optoelectronic technologies. Presented here is a comprehensive theoretical analysis of the structural, topological, and NLO features of 1-methylurea butanedioic acid (MUBA) alongside solvent effects (water, DMSO, and benzene) using the DFT method at the B3LYP(D4)/6–311++G(d,p) level. Geometric and infrared parameters were calculated and compared with experimental values. The analysis using atoms in molecules (AIM) and the independent gradient model (IGM) reveals the presence of two noncovalent intermolecular interactions: N_4–$H_{16}\cdots O_{12}$ and O_6–$H_{25}\cdots O_3$, which stabilize the crystal structure. The natural bond orbital (NBO) analysis reveals that the $LP(1)N_4 \longrightarrow \pi^*(C_2\text{-}O_3)$ interaction is the most stabilizing and is enhanced in solvent environments. NLO data show that the first (β_{tot}) and second ($\langle\gamma\rangle$) hyperpolarizability values of MUBA are approximately 0.6–1.1 and 8.3–17.0 times higher than those of urea. In addition, the quadratic and cubic responses of MUBA are significantly reduced and increased, respectively, in solvent environments. Based on its NLO susceptibilities, MUBA exhibits SHG, EOPE, OKE, and EFISHG properties, suggesting its potential application in the production of optoelectronic devices and optical limiting. This study enhances our understanding of the factors influencing the NLO behaviour of organic crystals, providing valuable insights for designing materials with enhanced NLO characteristics. The implications extend to industries such as telecommunications and computing, where faster data transmission rates are in high demand.

1. Introduction

In recent years, there have been numerous theoretical computations of the (hyper) polarizabilities of molecular systems focused on designing novel compounds for nonlinear optical (NLO) applications [1–7]. Despite significant advances in the use of NLO materials in areas such as photonics, laser technology, and optoelectronics, where light is utilized for information transmission, the search for novel NLO systems that can better meet the needs of these sectors continues to be a major focus [1, 7–10]. Current literature indicates some developments in new and improved NLO materials (organic, semiorganic, and inorganic) with good optical damage tolerances and the ability for optical bandwidth conversion [8–15]. In general, factors such as conjugated length, molecule conformation, and intramolecular charge transfer influence NLO features [16]. Pegu [17] conducted a DFT study on the solvent effects on the nonlinear optical properties of novel paranitroaniline derivatives. This study was carried out in various dielectric

constant media, including vacuum, chloroform, ethanol, and DMSO. The findings revealed that the solvents enhance the NLO properties of the molecules as their dielectric constants increase. Among the many compounds explored for their potential applications as NLO chromophores, urea and its single-crystal derivatives are also being considered [18]. Urea has a reasonably high laser damage limit and large nonlinear optical constants [19]. Slow evaporation and seed rotation techniques were used to synthesize and grow the organic nonlinear optical crystal, urea p-nitrophenol, for its potential use as an optical limiter, as reported by Suresh et al. [20]. The Z-scan approach outcome reveals that the tests are suitable for studies on optical limiters due to their optical nonlinearity. Suresh et al. [21] also investigated the third-order optical nonlinearity properties of N-methylurea succinic acid crystal, termed 1-methylurea butanedioic acid (MUBA) herein (see Figure 1), and its suitability for laser limiting applications.

Their findings indicate that the sample studied can effectively regulate optics to shield responsive sensing devices and components from beam failure. Although they experimentally investigated the third-order optical nonlinearity parameters of MUBA, comprehensive theoretical studies to support the results and gain insights into the impact of solvent media have not been conducted. Therefore, a detailed theoretical investigation of the NLO activity of MUBA alongside solvent effects is necessary to tailor its properties for specific applications. Like other intrinsic parameters, the NLO performance of a compound is influenced by its surroundings [22]. Janjua et al. [23] reported that the electronic and chemical qualities of a compound change in the presence of solvents. They also showed that the main way the environment affects the NLO signal of compounds is through solute polarization caused by the solvent. Theoretical techniques such as density functional theory (DFT) can be used to study the influence of solvents on the NLO activity of MUBA conveniently. Understanding the relationship between a compound's electronic structure and photophysical characteristics using DFT has become cost-effective and time-efficient [8, 24]. H-bond formations between the 1-methyl urea (MU) and butanedioic acid (BA) moieties of MUBA (N–H···O and O–H···O) are possible, which can stabilize the molecule. Similarly, MU and BA will engage in intramolecular charge transfer (ICT) throughout the molecule, with each acting as a donor or acceptor. In addition, the structure of MUBA is noncentrosymmetric and can function as a nonlinear optical (NLO) material. Materials with NLO properties can be useful in areas such as telecommunications, data storage, and optical information processing [1–10, 25, 26].

With this in mind, the main focus of this piece was to theoretically explore the nonlinear optical (NLO) features of MUBA, as well as the influence of three solvents (water, DMSO, and benzene). To achieve this, structural, electron-density-based topology (IGM, AIM) and NBO analyses were performed using the DFT method. The finite-field (FF) approach was employed to compute static hyperpolarizabilities, as well as the following frequency-dependent (dynamic) NLO properties: second-harmonic generation

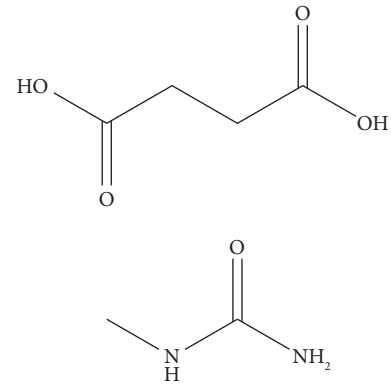

Figure 1: The chemical structure of 1-methylurea butanedioic acid (MUBA) crystal.

(SHG), electro-optical Pockels effect (EOPE), electric-field-induced second-harmonic generation (EFISHG), and optical Kerr effect (OKE). The motivation for this study stems from the importance of nonlinear optical materials in various technological applications, including optical communications, data processing, and imaging. In addition, by studying the effects of structural modifications, topological changes, and solvent interactions, we can gain insight into the components that determine a material's NLO response. This understanding can guide the design and development of NLO materials with desired qualities. Furthermore, this computational analysis will provide a cost-effective and efficient technique for investigating the material's NLO behaviour, offering vital information that can direct experimental efforts and aid in the interpretation of experimental results. The present work will make significant contributions to the field of nonlinear optics and material design. Firstly, by thoroughly investigating the structural and topological features that influence the nonlinear optical response, we enhance our understanding of the underlying factors governing the optical behaviour of this crystal. This knowledge is highly valuable for designing new optically active materials with enhanced functionalities using sound engineering principles. Secondly, our study goes beyond conventional analyses by considering solvent effects on nonlinear optical properties. By elucidating interactions between crystals and their surrounding solvent environments, we provide insights into how solvation influences optical response information crucial for applications involving solvated systems. Furthermore, the current work showcases methodological advancements by incorporating state-of-the-art computational techniques such as density functional theory (DFT) and time-dependent density functional theory (TD-DFT). These advancements contribute significantly to developing accurate computational tools for predicting and understanding complex molecular systems' optical behaviour. Finally, practical implications from our findings extend across various fields including optoelectronics, photonics, and nonlinear optics. The knowledge gained from this study can be leveraged to design efficient materials for signal processing in

optoelectronics, data storage, and communication technologies, among other areas.

2. Computational Details

The Avogadro 1.1.1 tool [27] was utilized to generate the input files for the computations. The ORCA 5.0.3 software [28] was then employed to perform geometry optimization and vibrational frequency calculations on MUBA in the gaseous state using Becke's three-Lee-Yang-Parr parameter (B3LYP) functional [29] and the 6–311++G(d,p) Pople basis set. Only real frequencies were observed, indicating the stability of the optimized geometry of MUBA is stable. To account for long-range interactions neglected by B3LYP, the D4 correction term [30] was incorporated. In addition, the resolution-of-the-identity (RI-J) [31] and chain-of-spheres (COSX) [32] approximations with an appropriate auxiliary basis set were applied to expedite the calculations. Solvent effects on all properties were investigated using water (protic solvent, dielectric constant, $\varepsilon = 80$), dimethyl sulfoxide (DMSO) (aprotic solvent, $\varepsilon = 46.83$), and benzene (nonpolar solvent, $\varepsilon = 2.27$). The universal SMD solvation model [33] implemented in both ORCA and Gaussian software was used to consider solvent effects at the B3LYP/6–311++G(d,p) level.

Within the framework of the quantum theory of atoms in molecules (QTAIM), topological investigations of the electron density were conducted using the Multiwfn 3.3.9 program [34] in all study media. The independent gradient model (IGM) analysis was also utilized with Multiwfn and visualised with VMD [35]. Topological electron density studies were carried out in all cases investigated using wavefunction (WFN) files generated from the optimized geometries. IGM (denoted by ∂g) has been used to characterize noncovalent interactions and is determined as the difference between the noninteractive (g^{IGM}) and the true system (g) as follows [36, 37]:

$$\partial g(r) = g^{IGM}(r) - \mathrm{g(r)}. \tag{1}$$

This scheme provides a method for automatically extracting the interactions between two specific fragments (∂g^{inter}), within each of these fragments (∂g^{intra}), or involving two atoms (∂g^{pair}). The use of ∂g^{inter} has been chosen because we are particularly interested in intermolecular interactions.

The NBO analysis was conducted in terms of the second-order perturbation energy ($E^{(2)}$) [38] at the B3LYP/6–311++G(d,p) level using the NBO 3.1 module [39] of the Gaussian 09 package. This analysis was performed to obtain information on donor-acceptor interactions. $E^{(2)}$ values were calculated for the donor-acceptor interactions using the following equation:

$$E^{(2)} = q_i \frac{F_{ij}^2}{\varepsilon_i - \varepsilon_j}, \tag{2}$$

where q_i is the orbital occupancy, ε_i and ε_j are orbital energies, and F_{ij} is the off-diagonal NBO Fock matrix element [40].

The NLO susceptibilities and attributes of MUBA were determined with using the Gaussian 09 (revision D) package [41]. This was based on the ORCA-optimized geometries at the B3LYP/6–311++G(d,p) level, employing the finite field technique. The static second (β_{tot}) and third-order polarizabilities ($\langle\gamma\rangle$) and the vector constituent of the dynamic second-order polarizability (β_{vec}) were obtained using the following equation [8,10]:

$$\beta_{\mathrm{tot}} = \left(\beta_x^2 + \beta_y^2 + \beta_z^2\right)^{1/2}, \tag{3}$$

where $\beta_x = (\beta_{xxx} + \beta_{xyy} + \beta_{xzz})$, $\beta_y = (\beta_{yyy} + \beta_{yzz} + \beta_{yxx})$, and $\beta_z = (\beta_{zzz} + \beta_{zxx} + \beta_{zyy})$ with β_{xxx}, β_{xyy}, β_{xzz}, β_{yyy}, β_{xxy}, β_{zzz}, β_{xxz}, and β_{yyz} representing the tensor components for the first hyperpolarizability.

$$\langle\gamma\rangle = \frac{1}{5}\left(\gamma_{xxxx} + \gamma_{yyyy} + \gamma_{zzzz} + 2\gamma_{xxyy} + 2\gamma_{xxzz} + 2\gamma_{yyzz}\right), \tag{4}$$

with γ_{xxxx}, γ_{yyy}, γ_{zzzz}, γ_{xxyy}, γ_{xxzz}, and γ_{yyzz} representing the tensor components of the second hyperpolarizability.

$$\beta_{vec} = \left(\beta_x^2 + \beta_y^2 + \beta_z^2\right)^{1/2}, \tag{5}$$

where $\beta_i (i = x, y, z)$ is given by the following equation:

$$\beta_i = \left(\frac{1}{3}\right) \sum_{j=x.y.z} \left(\beta_{ijj} + \beta_{jij} + \beta_{jji}\right). \tag{6}$$

The vector component of the first hyperpolarizability horizontal to the dipole moment of MUBA, as well as its dynamic first and second hyperpolarizabilities, were determined at a wavelength of 1064 nm.

3. Results and Discussion

3.1. Minimum Geometry of MUBA Crystal. The minimum geometries of MUBA in all investigated media are shown in Figure 2. The corresponding optimized Cartesian coordinates can be found in Tables S1–S5 of the associated supplementary file (SF).

Figure 2 illustrates the presence of two intermolecular hydrogen bonds: N_4-$H_{16}\cdots O_{12}$ and O_6-$H_{25}\cdots O_3$ in MUBA (in the gas phase, DMSO, and benzene) and O_6-$H_{25}\cdots O_3$ in the aqueous phase. These bonds form between the MU and BA moieties of MUBA and significantly contribute to the molecule's stability.

Presented in Table 1 is a comparison of some experimental (expt) [21] and theoretical (calc) geometric parameters of MUBA.

Table 1 reveals that the calculated geometric parameters closely align with their experimental counterparts. To further compare these bond lengths and angles, a curve fitting analysis was conducted. Equation (7) shown below was derived with a correlation coefficient (R^2), approaching unity.

$$\mathrm{calc} = 0.99533\mathrm{expt} + 0.09995, R^2 = 0.99939. \tag{7}$$

Based on the correlation coefficient value obtained, the computed and measured readings align, confirming the optimized geometry of MUBA and the appropriateness of

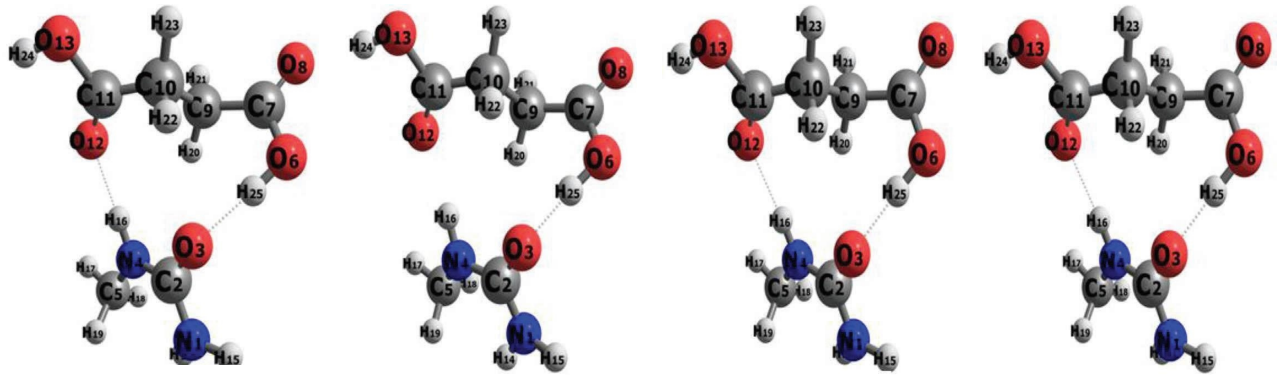

(a) (b) (c) (d)

Figure 2: The minimum geometries of MUBA: (a) gas, (b) water, (c) DMSO, and (d) benzene.

Table 1: Some geometric parameters for MUBA.

	Expt.[a]	Gas[b]	Water	DMSO	Benzene
Bond length[c] (Å)					
C_7-O_8	1.209	1.206	1.222	1.214	1.210
C_7-O_6	1.306	1.342	1.336	1.335	1.337
O_6-H_{25}	0.820	0.986	1.003	0.999	0.992
C_2-O_3	1.254	1.242	1.264	1.256	1.249
N_1-C_2	1.331	1.372	1.353	1.361	1.365
N_4-C_5	1.434	1.451	1.459	1.456	1.453
C_7-C_9	1.501	1.526	1.511	1.518	1.522
C_9-H_{20}	0.970	1.091	1.090	1.091	1.091
C_9-H_{21}	0.970	1.090	1.090	1.090	1.090
C_9-C_{10}	1.506	1.538	1.537	1.538	1.538
C_5-H_{17}	0.960	1.089	1.089	1.090	1.090
C_5-H_{18}	0.960	1.097	1.095	1.095	1.096
C_5-H_{19}	0.960	1.095	1.093	1.095	1.096
Bond angle[c] (°)					
C_7-O_6-H_{25}	109.5	112.3	113.2	112.8	112.6
C_2-N_4-C_5	125.9	125.6	124.3	125.5	125.6
C_2-N_4-H_{16}	117.1	115.1	115.0	115.8	115.4
C_5-N_4-H_{16}	117.1	119.0	117.1	118.4	118.4
C_2-N_1-H_{14}	120.0	121.6	121.9	121.6	121.8
C_2-N_1-H_{15}	120.0	115.5	117.2	116.9	116.4
C_7-C_9-H_{20}	109.0	109.9	109.1	109.5	109.7
C_7-C_9-H_{21}	109.0	107.3	108.1	108.1	107.7
O_8-C_7-O_6	123.3	121.2	119.5	120.4	120.8
O_8-C_7-C_9	124.1	122.7	123.3	123.1	122.9
O_3-C_2-N_1	120.0	120.9	120.6	120.9	120.9
O_3-C_2-N_4	120.8	121.9	121.1	121.4	121.5
N_4-C_2-N_1	119.3	117.3	118.4	117.7	117.5
N_4-C_5-H_{17}	109.5	108.3	108.0		108.1
Dihedral angle[c] (°)					
C_9-C_7-O_6-H_{25}	—	1.7	1.1	1.7	1.4
C_{11}-C_{10}- C_9-C_7	—	172.0	171.9	171.8	172.1
O_3-C_2-N_4-C_5	—	174.6	173.2	176.0	174.2
C_5-N_4-C_2-N_1	—	3.8	7.3	2.2	4.4
O_3-C_2-N_4-H_{16}	—	0.5	15.2	1.5	3.2
H – bond[c] (Å)					
N_4-$H_{16}\cdots O_{12}$	—	1.922	2.045	1.967	1.945
O_6-$H_{25}\cdots O_3$	—	1.704	1.613	1.614	1.656

[a] Experimental values obtained from [21]. [b] Computed geometric parameters (this work). [c] Atom labels are displayed in Figure 2.

the applied level. These results also indicate that the solvent environment does not affect geometric properties of MUBA.

In addition, key dihedral angles, including C_9-C_7-O_6-H_{25}, C_{11}-C_{10}-C_9-C_7, O_3-C_2-N_4-C_5, C_5-N_4-C_2-N_1, and O_3-C_2-N_4-H_{16} are provided. Ideally, these angles should either be 0° or 180°. Clearly, these values deviate from 0° or 180° for perfect planarity. However, it is evident that these values deviate from the ideal range. For example, the O_3-C_2-N_4-H_{16} angle in water (15°) deviates from 0° due the elongated N_4-$H_{16}\cdots O_{12}$ distance, which prevents the complete molecule from twisting.

Also presented in Table 1 are the computed intermolecular hydrogen bond lengths (N_4-$H_{16}\cdots O_{12}$ and O_6-$H_{25}\cdots O_3$) of MUBA in all study media. The results show that in all cases, N_4-$H_{16}\cdots O_{12}$ is longer than O_6-$H_{25}\cdots O_3$ by approximately 0.22 and 0.36 Å in gas and solvent phases, respectively. This suggests that O_6-$H_{25}\cdots O_3$ plays a more significant role in stabilizing the molecule than N_4-$H_{16}\cdots O_{12}$.

3.2. Infrared Spectral Evaluation. Table 2 lists some calculated (scaled) gaseous phase infrared (IR) frequencies for the MUBA crystal in all study media, along with their likely assignments and the corresponding experimental values from [21].

Due to electron correlation effects and basis set limitations, the DFT/B3LYP method significantly overestimates normal frequencies [42]. A scaling factor of 0.9614 was utilized in this study to adjust the frequencies calculated using the DFT/B3LYP method. The experimental (IR) and calculated scaled wavenumbers of the MUBA crystal were compared. The linear regression analysis resulted in the following equation:

$$\boldsymbol{\nu}_{\mathbf{cal}} = 0.9501\boldsymbol{\nu}_{\mathbf{exp}} + 148.905, R^2 = 0.9992. \quad (8)$$

The high R^2 value of 0.99916 indicates a perfect agreement between the measured and computed frequencies, highlighting the accuracy of the chosen level of theory and the optimized structures. The NH_2 vibration was experimentally predicted at

Table 2: Calculated IR frequencies for MUBA crystal and the corresponding experimental IR frequencies.

Media	$\nu(NH_2)$		$\nu(C-H)$		$\nu(O-H)$		$\nu(C-N)$		$\nu(C-O)$ stretching		$\nu(C-O)$ bending	
	ν_{exp}	ν_{cal}	ν_{exp}	ν_{cal}	ν_{exp}	ν_{cal}	ν_{exp}	ν_{cal}	ν_{exp}	ν_{cal}	ν_{exp}	ν_{cal}
Gas	3438	3451	2848	2883	—	3595	1429	1277	1264	1154	553	484
DMSO	—	3436	—	2901	—	3541	—	1375	—	1226	—	534
Water	—	3382	—	2914	—	3567	—	1375	—	1209	—	530
Benzene	—	3305	—	2894	—	3567	—	1377	—	1224	—	534

3438 cm^{-1} and theoretically obtained at 3451 cm^{-1}, demonstrating a good correlation. The C-O bond stretching vibrations at 1264 cm^{-1} were validated by bands corresponding assigned to the computed vibrational frequency at 1154 cm^{-1}. These results also suggest that solvation leads to an increase in the wavenumbers of the C-N, C-H, and C-O vibrations.

3.3. Topological Analyses

3.3.1. Analysis of Quantum Theory of Atoms in Molecules (QTAIM). The QTAIM analysis was performed to gain specific knowledge about the type and strength of the interactions between the fragments that constitute MUBA. Topological parameters at bond critical points (BCPs) for MUBA were computed at the RIJCOSX-B3LYP(D4)/6–311++G(d,p) level in all media and are summarised in Table 3.

The findings reveal that in all studied conditions, a bond critical point (BCP) occurs between atoms O_{12} and H_{16}, and O_3 and H_{25} atoms of the 1-methylurea and butanedioic acid moieties. This observation is consistent with that from Figure 2. In each case, the ρ(r) values at the BCP are less than 0.1 a.u., while the $\nabla^2\rho\ (r)$ values are all positive, suggesting that the intermolecular H-bonds in MUBA in all study media are noncovalent in nature. This is in accordance with Koch and Popelier's H-bond formation requirements. The results also show that $-G\ (\mathbf{r}_{BCP})/V\ (\mathbf{r}_{BCP}) > 1$ for N_4-$H_{16}\cdots O_{12}$ and $0.5 < -G\ (r)/V\ (r) < 1$ for O_6-$H_{25}\cdots O_3$, implying that N_4-$H_{16}\cdots O_{12}$ is noncovalent, whereas O_6-$H_{25}\cdots O_3$ is partially covalent. In addition, the results indicate that in MUBA, the O_6-$H_{25}\cdots O_3$ interaction is stronger than N_4-$H_{16}\cdots O_{12}$ by about 6.074 and 10.861 kcal/mol in the gaseous phase and solvent media, respectively. This observation aligns with the geometric parameters. The QTAIM analysis provides additional evidence of the existence of H-bonds in MUBA, contributing to the molecule's stabilization. Figure 3 displays the molecular graphs showing the bond critical points (BCPs) of H-bonds in MUBA.

In addition to the N_4-$H_{16}\cdots O_{12}$ and O_6-$H_{25}\cdots O_3$ bonds, the C_{10}-$H_{22}\cdots O_3$ and $H_{16}\cdots H_{20}$ bonds are observed in figure above in all study environments (except in the gaseous phase). All of these bonds play a role in stabilizing the molecule by preventing free rotation and twisting of the molecule.

3.3.2. Independent Gradient Model (IGM) Analysis Based on Promolecular Densities. Here, interfragment interactions for the MUBA crystal were calculated using promolecular densities via the independent gradient model (IGM). The IGM representation employs a color code to distinguish between attractive and repulsive noncovalent interactions based on the sign of the middle eigenvalue of the Hessian. Yellow and red represent strong and weak repulsive interactions, while blue and green represent weak and strong attractive interactions, respectively. Figure 4 shows the color-filled map, 2D scatter plots, and 3D isosurface for interfragment interactions of the ∂g gradient-based descriptor for MUBA in the gaseous and solvent phases.

Table 3: The electron density, its Laplacian, the ratio of the kinetic energy density, and potential energy density at the BCP, along with the interatomic interaction energy for MUBA.

Media	Hydrogen bond	P (r)	$\nabla^2\rho\ (r)$	$-G(r)/V(r)$	E_{int}
Gas	O_6–$H_{25}\cdots O_3$	0.0408	0.1406	0.9588	−12.019
	N_4–$H_{16}\cdots O_{12}$	0.0253	0.0952	1.1279	−5.945
Water	O_6–$H_{25}\cdots O_3$	0.0526	0.1514	0.8561	−16.676
	N_4–$H_{16}\cdots O_{12}$	0.0194	0.0717	1.1829	−4.116
DMSO	O_6–$H_{25}\cdots O_3$	0.0519	0.1559	0.8686	−16.586
	N_4–$H_{16}\cdots O_{12}$	0.0231	0.0861	1.1482	−5.212
Benzene	O_6–$H_{25}\cdots O_3$	0.0461	0.1496	−0.9124	−14.226
	N_4–$H_{16}\cdots O_{12}$	0.0242	0.0906	1.1372	−5.576

$\rho\ (r)$: the electron density (in a.u.); $\nabla^2\rho\ (r)$: Laplacian of the electron density (in a.u.); $-G(r)/V(r)$: the ratio of the kinetic energy density and potential energy density; E_{int}: the interatomic interaction energy (in kcal/mol).

Figure 4(a) shows the color-filled scatter plot of ∂g for the MUBA crystal mapped between 0.0 and 0.2 in all media. It can be observed from the figure that all chemical bond areas have higher ∂g values as reflected in white. However, some dotted red regions exist in the molecules in all media, indicating that the function ∂g has a lower value than the chemical bond area. Figure 4(b) shows a 2D scatter plot of ∂g^{inter} against sign $(\lambda_2)\ \rho$ $(\mathbf{r})$ for the MUBA crystal. The spikes appear at −0.04 to 0.04 a.u. in all media, indicating a region of high electron density. The height is about 0.110 a.u. (∂g^{inter}) and implies the presence of hydrogen bonds. The corresponding 3D isosurfaces are illustrated in Figure 4(c). The outcome of the IGM evaluation confirms the presence of two intermolecular interactions: N_4-$H_{16}\cdots O_{12}$ and O_6-$H_{25}\cdots O_3$. The blue around the centre of the isosurface corresponding to the O_6-$H_{25}\cdots O_3$ interaction is broader and darker than that corresponding to the N_4-$H_{16}\cdots O_{12}$ interaction, which is in line with the observations from the AIM evaluation.

3.4. Natural Bond Orbital Investigation of the MUBA Crystal.

NBO provides a precise method for studying inter- and intramolecular interactions, as well as conjugative interactions and charge transfer in molecules [43]. The

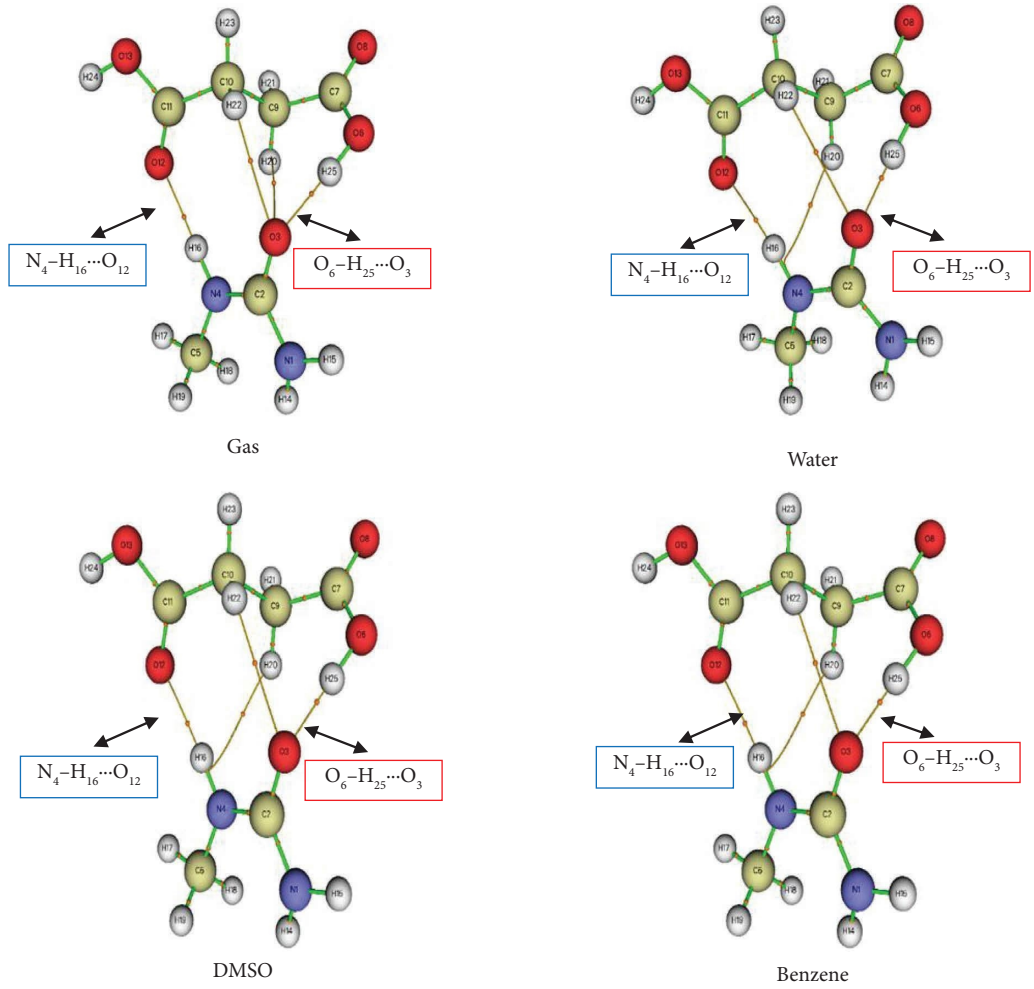

Figure 3: Molecular graphs of MUBA crystal in gas, water, DMSO, and benzene presenting the H-bond interactions.

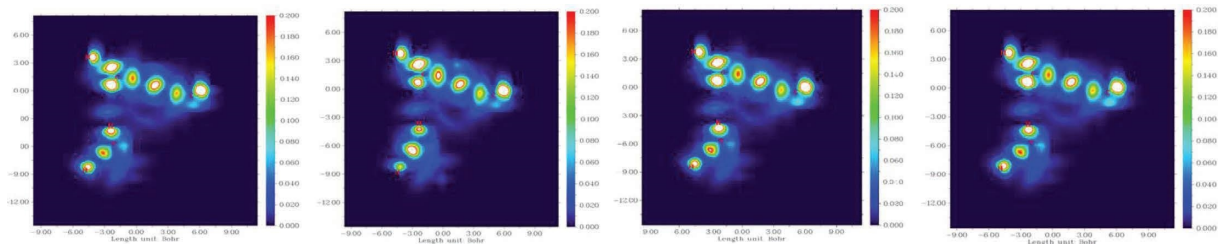

(a)

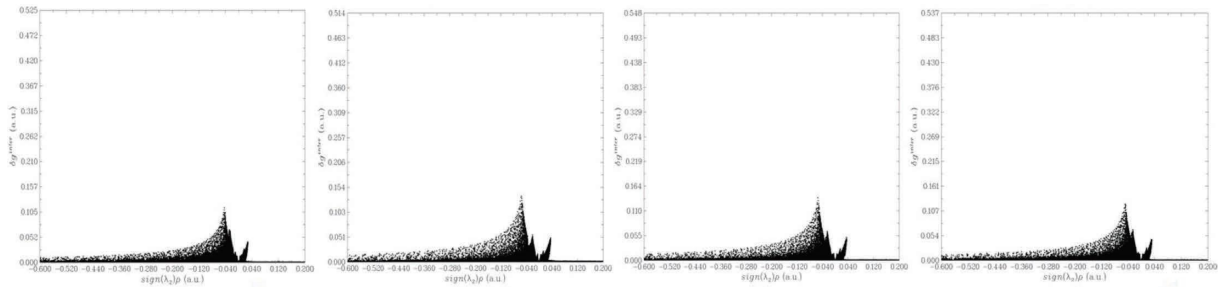

(b)

Figure 4: Continued.

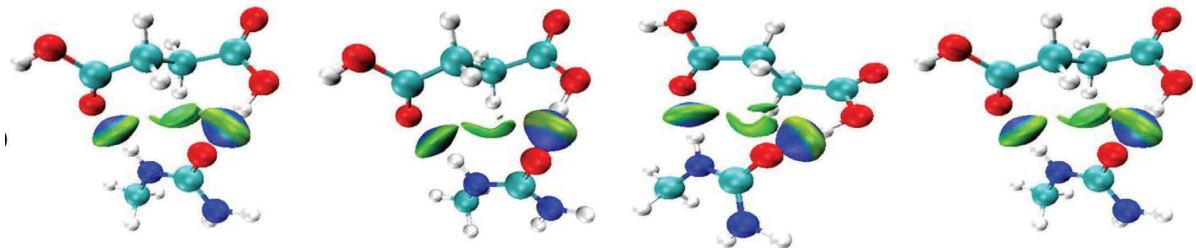

(c)

Figure 4: (a) Color-filled map, (b) 2D scatter plot, and (c) 3D isosurface for interfragment interactions of ∂g gradient-based descriptor for MUBA in the gaseous and solvent phases.

possible donor-acceptor interactions of MUBA along with their stabilization energies are reported in Table 4.

Generally, the higher the $E^{(2)}$ value, the stronger the donor-acceptor NBO interaction, leading to increased ICT throughout the system [44, 45]. Therefore, the donor LP(1) $N_4 \longrightarrow \pi^*(C_2\text{-}O_3)$ acceptor interaction has the highest stabilization energy of 55.25, 62.15, 64.19, and 65.32 kcal/mol (respectively, in vacuum, benzene, DMSO, and water). It is evident that the solvent medium, especially polar solvents, enhances the NBO stabilization energies of the compounds studied, which can subsequently increase their second hyperpolarizabilities. In addition, the interactions between the lone pairs (LP) and antibonding (σ^*, π^*) orbitals: $LP(1)N_1 \longrightarrow \pi^*(C_2\text{-}O_3)$, $LP(1)N_4 \longrightarrow \pi^*(C_2\text{-}O_3)$, $LP(2)O_6 \longrightarrow \pi^*(C_7\text{-}O_8)$, $LP(2)O_8 \longrightarrow \sigma^*(O_6\text{-}C_7)$, and $LP(2)O_{13} \longrightarrow \pi^*(C_{11}\text{-}O_{12})$, exhibit significant stabilization energy in all studied environments compared to bonding (σ, π) and antibonding (σ^*, π^*) contributions: $\sigma(N_4\text{-}H_{16}) \longrightarrow \sigma^*(N_1\text{-}C_2)$ and $\pi(C_2\text{-}O_3) \longrightarrow \sigma^*(C_2\text{-}O_3)$.

3.5. Atomic Point Charge Analysis. Evaluation of the variation of polarization and ICT was achieved by estimating atomic point charges for the MUBA crystal in all investigation conditions using the Hirshfeld population analysis scheme. Figure 5 illustrates the total Hirshfeld charges on the atoms of the two MUBA moieties.

Figure 5 demonstrates that the BA group has an overall positive charge (electron deficient) for MUBA in all examined media, while the MU moiety has a net negative charge (richer in electrons). This indicates that ICT is feasible in MUBA. In addition, this figures out that the solvent media induce larger charge separation, suggesting that photo-induced ICT is more likely to occur in the solution. MUBA is a noncentrosymmetric system where the BA and MU moieties, respectively, serve as the electron-acceptor and donor, as shown by atomic point charge studies. This donor-acceptor system is most likely to act as an NLO chromophore.

3.6. Reactivity Site Investigation for the MUBA Crystal. The identification of reactive sites allows for the determination of the most likely electron-donor and acceptor sites within a compound. Atoms with the most negative atomic charges are more likely to donate [46]. The net atomic charges under the framework of the Hirshfeld scheme are outlined in Table 5.

Table 4: Donor-acceptor interactions in MUBA and their stabilization energies in the gaseous and solvent phases.

Donor (i)[a]	Acceptor (j)[a]	$E^{(2)}$(kcal/mol)			
		Gas	Water	DMSO	Benzene
$\sigma(N_4\text{-}H_{16})$	$\sigma^*N_1\text{-}C_2$	4.78	4.77	4.77	4.78
$LP(1)N_1$	$\pi^*C_2\text{-}O_3$	36.27	58.81	47.33	45.21
$LP(1)N_1$	$\sigma^*C_2\text{-}O_3$	3.01	0.53	1.86	1.97
$LP(2)O_3$	$\sigma^*N_1\text{-}C_2$	20.76	17.94	19.65	19.95
$LP(2)O_3$	$\sigma^*C_2\text{-}N_4$	19.10	16.80	16.80	16.93
$LP(1)N_4$	$\pi^*C_2\text{-}O_3$	55.25	65.32	64.19	62.15
$\pi(C_2\text{-}O_3)$	$\sigma^*C_2\text{-}O_3$	18.79	8.11	12.56	13.33
$LP(2)O_6$	$\pi^*C_7\text{-}O_8$	48.48	52.53	51.41	51.17
$LP(2)O_8$	$\sigma^*O_6\text{-}C_7$	30.80	27.72	29.09	29.19
$LP(2)O_{13}$	$\pi^*C_{11}\text{-}O_{12}$	47.75	49.10	48.76	48.62

[a]Atom labels are displayed in Figure 2.

The results show that atoms $\mathbf{O_8}$, $\mathbf{O_3}$, and $\mathbf{O_{12}}$ are the most probable reactive sites, as they possess relatively larger negative charges. These atoms are ranked as follows in decreasing order of their negative charges: $\mathbf{O_8} > \mathbf{O_3} > \mathbf{O_{12}}$. Interestingly, in all study media, the highest negative atomic charge is found in an **O** atom, indicating its higher reactivity. In addition, these values increase as we transition from the gaseous phase to polar media and then to nonpolar media.

3.7. Nonlinear Optical Susceptibilities and Properties of MUBA. In this section, we discuss the nonlinear optical (NLO) susceptibilities and properties of MUBA in various media. See Tables S6–S10 of the SF for the tensor components of the static β_{tot}, the dynamic β_{tot}, and $\langle\boldsymbol{\gamma}\rangle$ of the different NLO susceptibilities and properties of MUBA.

3.7.1. First Hyperpolarizability of MUBA. Table 6 provides the values of the static first hyperpolarizability tensor (β_{tot}) for MUBA in different media, along with the isotropic averages of some tensor components along the x, y, and z directions.

The β_{tot} value of MUBA in all study media (except DMSO) is found to be 0.6–1.1 times greater than that of urea. This indicates that MUBA is a potent NLO material,

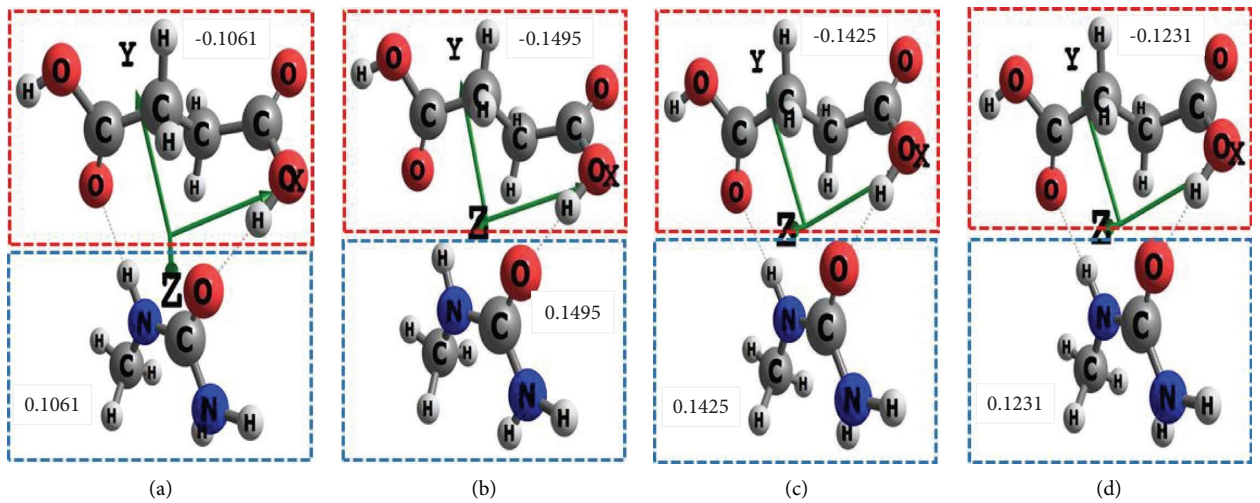

Figure 5: Total Hirshfeld charges borne by the 1-methylurea and butanedioic acid moieties of MUBA crystal: (a) gas, (b) water, (c) DMSO, and (d) benzene.

Table 5: Hirshfeld atomic charges of the MUBA crystal in all study media.

Atoms	Gas	Water	DMSO	Benzene
N_1	−0.1472	−0.1291	−0.1395	−0.1432
C_2	0.1927	0.1904	0.1865	0.1893
O_3	**−0.2887**	**−0.3470**	**−0.3150**	**−0.3021**
N_4	−0.0924	−0.0884	−0.0898	−0.0922
C_5	−0.0258	−0.0205	−0.0216	−0.0240
O_6	−0.1923	−0.2159	−0.2093	−0.2001
C_7	0.1989	0.2064	0.1964	0.1979
O_8	**−0.2941**	**−0.3834**	**−0.3407**	**−0.3188**
C_9	−0.0512	−0.0420	−0.0475	−0.0491
C_{10}	−0.0441	−0.0346	−0.0404	−0.0420
C_{11}	0.2292	0.2400	0.2313	0.2302
O_{12}	**−0.2515**	**−0.2853**	**−0.2598**	**−0.2566**
O_{13}	−0.1573	−0.1633	−0.1588	−0.1578
H_{14}	0.1186	0.1455	0.1410	0.1301
H_{15}	0.1315	0.1473	0.1422	0.1376
H_{16}	0.0922	0.0985	0.0903	0.0908
H_{17}	0.0546	0.0572	0.0577	0.0565
H_{18}	0.0342	0.0445	0.0471	0.0408
H_{19}	0.0364	0.0510	0.0436	0.0395
H_{20}	0.0305	0.0479	0.0392	0.0351
H_{21}	0.0411	0.0522	0.0485	0.0450
H_{22}	0.0491	0.0575	0.0520	0.0507
H_{23}	0.0475	0.0552	0.0521	0.0501
H_{24}	0.1783	0.2069	0.1912	0.1856
H_{25}	0.1098	0.1089	0.1031	0.1068

The bold values represent the most probable reactive sites.

Table 6: Selected constituents of the static first hyperpolarizability tensor (in a.u.) with the total value of the tensor (β_{tot}) for MUBA.

Media	β_{xxx}	β_{yyy}	β_{zzz}	β_x	β_y	β_z	$\beta_{tot} \times 10^{-30}$ esu
Gas	−119.58	−73.92	−19.89	−162.52	−112.07	−55.97	1.8
Water	−26.62	151.48	−95.59	−86.92	67.86	−184.01	1.9
DMSO	7.23	68.73	27.55	−16.91	−2.71	−55.25	0.5
Benzene	−71.25	−32.76	−4.96	−106.01	−95.07	−79.85	1.4
Urea[a]	0.04	88.59	0.00	−0.06	91.31	0.00	0.8

Conversion is 1 a.u. = 8.6393×10^{-33} esu. [a] Prototypical molecule used for comparison purposes.

Table 7: Constituents of the static second hyperpolarizability tensor (in a.u.) together with the average isotropic value of the tensor ($\langle \boldsymbol{\gamma} \rangle$) for MUBA.

Medium	γ_{xxxx}	γ_{yyyy}	γ_{zzzz}	γ_{xxyy}	γ_{xxzz}	γ_{yyzz}	$\langle \gamma \rangle \times 10^{-36}$ esu
Gas	33302.50	31039.10	14087.80	9742.74	5576.30	6963.93	12.4
Water	60906.70	46323.30	34203.30	16051.70	12416.10	13044.10	22.6
DMSO	62849.50	53229.80	32459.20	16987.90	12500.50	13512.30	23.6
Benzene	44393.00	39565.90	19004.50	12408.00	7751.99	8980.69	16.2
Urea[a]	11905.50	6994.24	6231.13	4341.06	2090.80	1468.40	4.1

Conversion factor: 1 a.u. = 0.50367×10^{-39} esu. [a] Prototypical molecule used for comparison purposes.

consistent with experimental findings [14]. The magnitude of β_{tot} is influenced by the surrounding environment. For example, the β_{tot} values in the gaseous phase, water, DMSO, and benzene are 1.8, 1.9, 0.5, and 1.4×10^{-30} esu, respectively. This suggests that the quadratic NLO response of MUBA is slightly reduced in the presence of a solvent, with a significant decrease observed in DMSO. This suggests that its second-order NLO properties will be low as well.

3.7.2. Second Hyperpolarizability of MUBA. Table 7 presents the data for the average static second hyperpolarizability tensor ($\langle \gamma \rangle$) of MUBA in different media, along with the isotropic values of several tensor components.

The $\langle \gamma \rangle$ values of MUBA are approximately 8.3 and 17.0 times higher than that of urea in the gaseous phase and solvents, respectively. The computed average $\langle \gamma \rangle$ values for MUBA are 12.4, 22.6, 23.6, and 16.2×10^{-36} esu in the gaseous phase, water, DMSO, and benzene, respectively. This indicates that the $\langle \gamma \rangle$ values are influenced by the environment. Unlike the quadratic NLO response, the cubic response of MUBA significantly increases in the presence of a solvent. This enhancement can be attributed to the strengthening of nonbonding orbital interactions in the solvent media (see the $E^{(2)}$ values). The $\langle \gamma \rangle$ data further confirms that MUBA is a potent NLO material.

3.7.3. The Vector Part of the First Hyperpolarizability (β_{vec}) of MUBA. Table 8 provides the computed vector components of the dynamic first hyperpolarizability (β_{vec}) of MUBA projected along the dipole moment axis at a wavelength of 1064 nm.

The β_{vec} values of MUBA in all media (except DMSO) at 1064 nm are larger than those of urea. This indicates that MUBA has a higher propensity to act as an NLO material. The dynamic first hyperpolarizability of MUBA is parallel to the dipole moment vector. Solvation reduces the β_{vec} value of MUBA at 1064 nm, suggesting that the presence of a solvent affects its NLO properties.

3.7.4. Nonlinear Optical Properties of MUBA. Table 9 presents the dynamic first hyperpolarizabilities of MUBA corresponding to the electro-optical Pockels effect (EOPE) and second-harmonic generation (SHG), as well as the dynamic second-order hyperpolarizabilities corresponding to electric-field-induced second-harmonic generation (EFISHG) and optical Kerr effect (OKE) in different media.

Table 8: Vector components of the quadratic polarizabilities of MUBA at 1064 nm.

Media	β_x	β_y	β_z	$\beta_{vec} \times 10^{-30}$ esu
Gas	−192.313	−156.812	−53.8483	2.2
Water	−60.4392	36.8813	−84.398	1.0
DMSO	−35.0836	−33.7126	−14.1191	0.4
Benzene	−126.623	−140.574	−29.9594	1.7
Urea[a]	−0.07525	94.28701	−0.02508	0.8

[a] Prototypical molecule used for comparison purposes.

Table 9: Dynamic first and second hyperpolarizabilities of MUBA at 1064 nm.

	SHG[a]	EOPE[a]	OKE[b]	EFISHG[b]
Gas	2.08	1.89	13.28	14.93
Water	1.23	1.35	18.30	17.69
DMSO	0.52	0.54	20.45	20.58
Benzene	1.65	1.51	17.39	19.50
Urea[c]	0.95	0.85	11.39	5.24

SHG: second-harmonic generation; EOPE: electro-optical Pockels effect; EFISHG: electric-field-induced second-harmonic generation; OKE: optical Kerr effect. [a] value $\times 10^{-30}$ esu; [b] value $\times 10^{-36}$ esu; [c] prototypical molecule used for comparison purposes.

The SHG and EOPE values of MUBA in all media (except DMSO) are higher than those of urea, indicating its suitability for these NLO processes. These properties are higher in the gaseous phase and lower in DMSO. The EFISHG and OKE values of MUBA in all media are significantly higher than those of urea. Interestingly, these values are greater in solvents compared to vacuum, which is consistent with the observations from the $\langle \gamma \rangle$ susceptibility.

Overall, the results demonstrate that MUBA exhibits strong NLO properties and has potential applications in the field of optoelectronics.

4. Conclusion

A computational evaluation of the structural and electronic-density-based analyses of 1-methylurea butanedioic acid (MUBA) crystal as well as its NLO properties and the effects of solvents (protic, aprotic, and nonpolar) is reported herein. The DFT method was used alongside the B3LYP functional and the 6–311++G(d,p) basis. The simulated geometric and IR parameters were contrasted with their experimental counterparts, showing good agreement and demonstrating the viability of the level applied and the obtained optimized structures. The N_4–$H_{16}\cdots O_{12}$ and O_6–$H_{25}\cdots O_3$ intermolecular interactions,

which significantly aid in stabilizing the molecule, are confirmed by the AIM and IGM analyses. According to the NBO analysis, the $LP(1)N_4 \longrightarrow \pi^* C_2\text{-}O_3$ interaction contributes the most stabilization energy, which is increased in solvent media. The Hirshfeld scheme predicts that MUBA is a noncentrosymmetric system composed of the 1-methylurea (MU) and butanedioic acid (BA) moieties as electron donor and acceptor groups, respectively. The results also show that MUBA exhibits NLO susceptibilities in both the gaseous phase and in solvent media. The β_{tot} value of MUBA in all study media (except in DMSO) is 0.6-1.1-fold greater than urea (0.8×10^{-30} esu). In addition, the magnitude of MUBA's β_{tot} is affected by the surrounding environment, with varying values in different media. For the first hyperpolarizability, these susceptibilities are higher in the gaseous phase, while for the second hyperpolarizability, they are higher in the solvent (especially polar) media. The results also indicate that the dynamic first hyperpolarizability of MUBA in all media has a vector component that is positive and parallel to the dipole moment vector. Analyses of the dynamic second- and third-order polarizabilities at 1064 nm reveal properties such as SHG, EOPE, EFISHG, and OKE. MUBA can aid in the design of optoelectronic devices due to its NLO susceptibilities and properties. The findings from this study contribute to the understanding of the crystal's properties and offer guidance for designing novel materials with tailored NLO characteristics, paving the way for future material designs with improved functionality in diverse industries that rely on optic technology such as the telecommunications or computing sectors where faster data transmission rates are always desirable outcomes.

Data Availability

The data used to support the study are included in the supplementary data file and within the article.

Conflicts of Interest

The authors declare that there are no conflicts of interest.

Acknowledgments

The authors thank the Cameroonian Ministry of Higher Education through the research modernization grants to lecturers of higher and tertiary education for their support.

Supplementary Materials

The supplementary material contains tables as a part of this work. Tables S1–S5 present the optimized geometrical coordinates of MUBA in different media, and Tables S6–S10 give the tensor components of the static β_{tot}, the dynamic β_{tot}, and $\langle \gamma \rangle$ of the different NLO susceptibilities and properties of MUBA. (*Supplementary Materials*)

References

[1] A. Linda Varghese, I. Abraham, and M. George, "DFT studies on nonlinear optical properties of N-[(naphthalen-5-yl) methyl]-4-nitrobenzamine," *Materials Today: Proceedings*, vol. 9, pp. 92–96, 2019.

[2] Z. Biglari, "Theoretical investigation of nonlinear optical properties of functionalized corannulene with B and N atoms," *Physica E: Low-Dimensional Systems and Nanostructures*, vol. 115, 2020.

[3] L. Kara Zaitri and S. M. Mekelleche, "Nonlinear optical activity of imino-dyes with furan, thiophene or thiazole moieties as π-conjugated bridge: a computational investigation," *Molecular Physics*, vol. 118, no. 18, Article ID e1761471, 2020.

[4] E. Rtibi and B. Champagne, "Density functional theory study of substitution effects on the second-order nonlinear optical properties of lindquist-type organo-imido polyoxometalates," *Symmetry*, vol. 13, no. 9, p. 1636, 2021.

[5] M. N. Arshad, M. Khalid, M. Asad, A. A. Braga, A. M. Asiri, and M. M. Alotaibi, "Influence of peripheral modification of electron acceptors in non-fullerene (O-IDTBR1)-based derivatives on nonlinear optical response: DFT/TDDFT study," *ACS Omega*, vol. 7, no. 14, pp. 11631–11642, 2022.

[6] K. Pielak, F. Bondu, L. Sanguinet, V. Rodriguez, B. Champagne, and F. Castet, "Second-order nonlinear optical properties of multi addressable indolino-oxazolidine derivatives: joint computational and hyper-Rayleigh scattering investigations," *Journal of Physical Chemistry C*, vol. 121, no. 3, pp. 1851–1860, 2017.

[7] R. Bano, M. Asghar, K. Ayub et al., "A theoretical perspective on strategies for modeling high performance nonlinear optical materials," *Frontiers in Materials*, vol. 8, 2021.

[8] M. Khalid, M. U. Khan, I. Shafiq et al., "NLO potential exploration for D–π–A heterocyclic organic compounds by incorporation of various π-linkers and acceptor units," *Arabian Journal of Chemistry*, vol. 14, 2021.

[9] M. Khalid, A. Ali, M. F. U. Rehman et al., "Exploration of noncovalent interactions, chemical reactivity, and nonlinear optical properties of piperidone derivatives: a concise theoretical approach," *ACS Omega*, vol. 5, no. 22, pp. 13236–13249, 2020.

[10] O. Concepcion, A. Ali, M. Khalid et al., "Facile synthesis of diversely functionalized peptoids, spectroscopic characterization, and DFT-based nonlinear optical exploration," *ACS Omega*, vol. 6, no. 40, Article ID 26016, 2021.

[11] N. S. Tasheh, N. K. Nkungli, and J. N. Ghogomu, "A DFT and TD-DFT study of ESIPT-mediated NLO switching and UV absorption by 2-(2′-hydroxy-5′-methylphenyl) benzotriazole," *Theoretical Chemistry Accounts*, vol. 138, no. 8, p. 100, 2019.

[12] C. T. Tedjeuguim, S. N. Tasheh, C. I. L. Alongamo, and J. N. Ghogomu, "A DFT and TD-DFT study of charge transport and non-linear optical properties of N-(4-methoxybenzylidene)isonicotinohydrazone, 2,2'-bipyridine and their Fe^{2+}, Ni^{2+}, Cu^{2+}, Pd^{2+} and Pt^{2+} complexes," *Journal of Chemical Sciences*, vol. 134, no. 3, pp. 70–15, 2022.

[13] D. E. Kiven, N. K. Nkungli, S. N. Tasheh, and J. N. Ghogomu, "In silico screening of ethyl 4-[(E)-(2-hydroxy-4-methoxyphenyl)methyleneamino]benzoate and some of its derivatives for their NLO activities using DFT," *Royal Society Open Science*, vol. 10, 2023.

[14] C. T. Tedjeuguim, S. N. Tasheh, and J. N. Ghogomu, "Theoretical investigation of the non-linear optical and charge transport properties of N-(4-methoxybenzylidene) isonicotinohydrazone and some of its derivatives: a DFT and TD-DFT study," *Advances in Materials Science and Engineering*, vol. 2023, p. 14, Article ID 6588603, 2023.

[15] M. Khalid, M. N. Arshad, S. Murtaza et al., "Enriching NLO efficacy via designing non-fullerene molecules with the modification of acceptor moieties into ICIF2F: an emerging

theoretical approach," *RSC Advances*, vol. 12, no. 21, pp. 13412–13427, 2022.

[16] M. Usman Khan, S. Nadeem, A. Fatima et al., "DFT molecular simulations for static, dynamic and solvent-dependent non-linear optical properties of triphenylamine-carbazole-based organic dyes with DDA framework," *Journal of Molecular Liquids*, vol. 391, 2023.

[17] D. Pegu, "Solvent effects on nonlinear optical properties of novel para-nitroaniline derivatives: a density functional approach," *International Journal of Science and Research*, vol. 3, pp. 469–474, 2014.

[18] A. Suresh, N. Manikandan, and G. Vinitha, "Review on growth and characterization of urea and urea derivative single crystals," *Brazilian Journal of Physics*, vol. 50, no. 2, pp. 192–213, 2020.

[19] A. Rathika and R. Ganapathi Raman, "Growth and characterization of an efficient nonlinear optical single crystal: urea p-nitrophenol," *Optik*, vol. 125, no. 12, pp. 2978–2982, 2014.

[20] A. Suresh, N. Manikandan, R. M. Jauhar, P. Murugakoothan, and G. Vinitha, "Growth and characterizaion of urea p-nitrophenol crystal: an organic nonlinear optical material for optoelectronic device application," *Applied Physics A*, vol. 124, no. 6, pp. 419–510, 2018.

[21] A. Suresh, N. Manikandan, and G. Vinitha, "N-Methylurea Succinic Acid (NMUSA): an optically non-linear organic crystal for NLO device application," *Materials Research Express*, vol. 6, no. 2, Article ID 25102, 2018.

[22] S. Kothavale, S. Katariya, and N. Sekar, "NLO phoric rigid pyrazino-phenanthroline donor-π-acceptor compounds: investigation of structural and solvent effects on non-linear optical properties using computational methods," *Optical Materials*, vol. 75, pp. 379–389, 2018.

[23] M. R. S. A. Janjua, A. Mahmood, and F. Ahmad, "Solvent effects on nonlinear optical response of certain tetramminеruthenium (II) complexes of modified 1, 10-phenanthrolines," *Canadian Journal of Chemistry*, vol. 91, no. 12, pp. 1303–1309, 2013.

[24] R. Peverati and D. G. Truhlar, "Quest for a universal density functional: the accuracy of density functionals across a broad spectrum of databases in chemistry and physics," *Philosophical Transactions of the Royal Society A: Mathematical, Physical and Engineering Sciences*, vol. 372, no. 2011, Article ID 20120476, 2014.

[25] P. S. Patil, S. R. Maidur, J. R. Jahagirdar, T. S. Chia, C. K. Quah, and M. Shkir, "Crystal structure, spectroscopic analyses, linear and third-order nonlinear optical properties of anthracene-based chalcone derivative for visible laser protection," *Applied Physics B*, vol. 125, no. 9, pp. 163–213, 2019.

[26] R. Zaier, F. Mahdhaoui, S. Ayachi, and T. Boubaker, "Prediction of structural, vibrational and nonlinear optical properties of small organic conjugated molecules derived from pyridine," *Journal of Molecular Structure*, vol. 1182, pp. 131–140, 2019.

[27] M. D. Hanwell, D. E. Curtis, D. C. Lonie, T. Vandermeersch, E. Zurek, and G. R. Hutchison, "Avogadro: an advanced semantic chemical editor, visualization, and analysis platform," *Journal of Cheminformatics*, vol. 4, p. 17, 2012.

[28] F. Neese, "Software update: the ORCA program system-Version 5.0," *WIREs Computational Molecular Science*, vol. 12, no. 5, Article ID e1606, 2022.

[29] A. D. Becke, "Density-functional thermochemistry. III. The role of exact exchange," *The Journal of Chemical Physics*, vol. 98, no. 7, pp. 5648–5652, 1993.

[30] E. Caldeweyher, C. Bannwarth, and S. Grimme, "Extension of the D3 dispersion coefficient model," *The Journal of Chemical Physics*, vol. 147, no. 3, Article ID 34112, 2017.

[31] F. Neese, "An improvement of the resolution of the identity approximation for the formation of the Coulomb matrix," *Journal of Computational Chemistry*, vol. 24, no. 14, pp. 1740–1747, 2003.

[32] F. Neese, F. Wennmohs, A. Hansen, and U. Becker, "Efficient, approximate and parallel Hartree-Fock and hybrid DFT calculations. A "chain-of-spheres" algorithm for the Hartree-Fock exchange," *Chemical Physics*, vol. 356, no. 1-3, pp. 98–109, 2009.

[33] A. V. Marenich, C. J. Cramer, and D. G. Truhlar, "Universal solvation model based on solute electron density and on a continuum model of the solvent defined by the bulk dielectric constant and atomic surface tensions," *The Journal of Physical Chemistry B*, vol. 113, no. 18, pp. 6378–6396, 2009.

[34] T. Lu and F. Chen, "Multiwfn: a multifunctional wavefunction analyzer," *Journal of Computational Chemistry*, vol. 33, no. 5, pp. 580–592, 2012.

[35] W. Humphrey, A. Dalke, and K. Schulten, "VMD: visual molecular dynamics," *Journal of Molecular Graphics*, vol. 14, no. 1, pp. 33–38, 1996.

[36] C. Lefebvre, G. Rubez, H. Khartabil, J.-C. Boisson, J. Contreras-García, and E. Hénon, "Accurately extracting the signature of intermolecular interactions present in the NCI plot of the reduced density gradient versus electron density," *Physical Chemistry Chemical Physics*, vol. 19, no. 27, Article ID 17928, 2017.

[37] C. Lefebvre, H. Khartabil, J.-C. Boisson, J. Contreras-García, J.-P. Piquemal, and E. Hénon, "The independent gradient model: a new approach for probing strong and weak interactions in molecules from wave function calculations," *ChemPhysChem*, vol. 19, no. 6, pp. 724–735, 2018.

[38] S. Maache, A. Bendjeddou, T. Abbaz, A. Gouasmia, and D. Villemin, "Molecular structure, hyperpolarizability, NBO and Fukui function analysis of a serie of 1,4,3,5-oxathiadiazepane-4,4-dioxides derived of proline," *Der Pharmacia Lettre*, vol. 8, pp. 27–37, 2016.

[39] E. D. Glendening, A. E. Reed, J. E. Carpenter, and F. Weinhold, *NBO, Version 3.1*, Gaussian. Inc, Pittsburgh, PA, USA, 2003.

[40] R. Renjith, Y. S. Mary, C. Y. Panicker et al., "Spectroscopic (FT-IR, FT-Raman), first order hyperpolarizability, NBO analysis, HOMO and LUMO analysis of 1,7,8,9-tetrachloro-10,10-dimethoxy-4-[3-(4-phenylpiperazin-1-yl)propyl]-4-azatricyclo[5.2.1.02,6]dec-8-ene-3,5- dione by density functional methods," *Spectrochimica Acta, Part A: Molecular and Biomolecular Spectroscopy*, vol. 124, pp. 500–513, 2014.

[41] M. Frisch, G. Trucks, and H. Schlegel, *Gaussian09*, Gaussian Inc, Wallingford, CT, USA, 2009.

[42] N. K. Nkungli, J. N. Ghogomu, L. N. Nogheu, and S. R. Gadre, "DFT and TD-dft study of bis[2-(5-amino-[1,3,4]-oxadiazol-2-yl) phenol] (diaqua) M(II) complexes [M = Cu, Ni and Zn]: electronic structures, properties and analyses," *Computational Chemistry*, vol. 03, no. 03, pp. 29–44, 2015.

[43] M. H. Miah, M. R. Hossain, M. S. Islam, T. Ferdous, and F. Ahmed, "A theoretical study of allopurinol drug sensing by carbon and boron nitride nanostructures: DFT, QTAIM, RDG, NBO and PCM insights," *RSC Advances*, vol. 11, no. 61, pp. 38457–38472, 2021.

[44] M. Karnan, V. Balachandran, M. Murugan, M. K. Murali, and A. Nataraj, "Vibrational (FT-IR and FT-Raman) spectra, NBO, HOMO-LUMO, molecular electrostatic potential

surface and computational analysis of 4-(trifluoromethyl) benzyl bromide," *Spectrochimica Acta Part A: Molecular and Biomolecular Spectroscopy*, vol. 116, pp. 84–95, 2013.

[45] V. D. Vitnik, Ž. J. Vitnik, N. R. Banjac, N. V. Valentić, G. S. Uśćumlić, and I. O. Juranić, "Quantum mechanical and spectroscopic (FT-IR, ^{13}C, ^{1}H NMR and UV) investigations of potent antiepileptic drug 1-(4-chloro-phenyl)-3-phenyl-succinimide," *Spectrochimica Acta Part A: Molecular and Biomolecular Spectroscopy*, vol. 117, pp. 42–53, 2014.

[46] T. A. Salman, D. S. Zinad, S. H. Jaber et al., "Effect of 1, 3, 4-thiadiazole scaffold on the corrosion inhibition of mild steel in acidic medium: an experimental and computational study," *Journal of Bio-and Tribo-Corrosion*, vol. 5, no. 2, pp. 48–11, 2019.